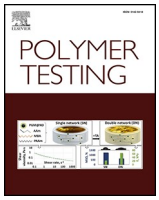
Polymer Testing 141 (2024) 108633



Contents lists available at ScienceDirect

Polymer Testing

journal homepage: www.elsevier.com/locate/polytest



Fabrication of advanced polyphenylene sulfide composites by in-situ grafting of sulfide silane and PCPA on glass fibers

Youngsung Cho [a], Jangwoo Cho [a], Jooheon Kim [a,b,*]

[a] School of Chemical Engineering & Materials Science, Chung-Ang University, 84 Heukseok-ro, Dongjak-gu, Seoul, Republic of Korea
[b] Department of Intelligent Energy and Industry, Graduate School, Chung-Ang University, Seoul, 06974, Republic of Korea

ARTICLE INFO

Keywords:
Thermal conductivity
Mechanical property
Surface treatment
Polymer-based composite
Polyphenylene sulfide

ABSTRACT

The energy crisis has driven increased adoption of electric vehicles (EVs) in the automotive sector, with a focus on lightweight engineering plastics (EPs) for fuel efficiency. This study aims to enhance the mechanical properties and thermal conductivity of EPs to address heat-related concerns in EVs and electronic devices. A hybrid filler (milled glass fiber, boron nitride, and graphene oxide) was introduced to polyphenylene sulfide (PPS), using a simultaneous grafting process with poly(catechol/polyamine) (PCPA) and silane additives. Filler aggregation in the resin matrix was overcome with surface-treatment agents such as Bis[3-(triethoxysilyl)propyl] tetrasulfide (Si69), catechol, and tetraethylenepentamine. PCPA polymerization on the filler surfaces bridged connections between fillers and silane molecules. The resulting surface-treated hybrid composite showed a 637 % increase in thermal conductivity (2.102 $Wm^{-1}K^{-1}$) and a 63.94 % increase in tensile strength (65.87 MPa) compared to the base matrix. Incorporating 40 wt% surface-treated mGF, 30 wt% raw BN, and 6 wt% surface-treated GO, along with PCPA and Si69 treatments, achieved this improvement. The hybrid filler composites significantly enhanced thermal conductivity and mechanical properties, providing a rapid and convenient solution to challenges in robustness and heat dissipation for electronic vehicles and devices.

1. Introduction

Addressing the global energy shortage and mitigating carbon emissions have become pressing issues [1,2]. Electric vehicles (EVs) run on electricity and are emerging as a viable substitute for conventional vehicles that rely on fossil fuels in the automobile industry [3]. The performance of electric vehicles (EVs), which are heavily dependent on their fuel efficiency, is closely tied to the weight of their chassis [4]. Consequently, there is an increasing focus on finding robust materials that can substitute current parts, lower the total weight of the vehicle (excluding the battery packs), and improve overall efficiency [5]. Engineering plastics (EPs) stand out as promising candidates in the automotive sector due to their processability, water resistance, cost-effectiveness, and lightweight nature [6–8].

However, challenges to the widespread adoption of EPs exist [9,10]. Polyamide (PA) has high moisture absorbance, and polycarbonate (PC) has issues associated with poor chemical stability [11,12]. During high-temperature molding, Polybutylene terephthalate (PBT) tends to undergo hydrolysis, while polyurethane is vulnerable to heat and polyvinyl chloride (PVC) is sensitive to cold temperatures [13,14]. These limitations hinder the broader application of EPs across various fields. Polyphenylene sulfide (PPS) has emerged as a remarkable super-engineering plastic that could solve these issues [15,16]. It can resist high temperatures, retain its chemical resistance, display flame-retardant properties, and uphold dimensional stability [17,18]. With a comparatively higher melting point of 275 °C, it stands out as a promising option for various applications [19,20].

Despite its merits, PPS has drawbacks in thermal conductivity compared to other engineering plastics. Accordingly, various thermally conductive fillers, including graphene [21,22], graphene oxide (GO) [23,24], carbon nanotubes [25,26], boron nitride (BN) [27,28], and aluminum nitride [29], have been introduced to enhance the thermal properties of polymers. Among these fillers, hexagonal-BN (h-BN) has attracted considerable attention as a ceramic filler and is frequently used in crafting high-thermal-conductivity composites [30]. Its appeal lies in its inherent features, namely a notable in-plane thermal conductivity of 185–300 $Wm^{-1}K^{-1}$, remarkable chemical stability, enhanced insulating characteristics, and weak dielectric properties [31,32]. These attributes are especially crucial in applications related to electronic devices [33–35].

* Corresponding author. School of Chemical Engineering & Materials Science, Chung-Ang University, 84 Heukseok-ro, Dongjak-gu, Seoul, Republic of Korea.
E-mail address: jooheonkim@cau.ac.kr (J. Kim).

https://doi.org/10.1016/j.polymertesting.2024.108633
Received 23 August 2024; Received in revised form 7 October 2024; Accepted 7 November 2024
Available online 8 November 2024
0142-9418/© 2024 The Authors. Published by Elsevier Ltd. This is an open access article under the CC BY-NC-ND license (http://creativecommons.org/licenses/by-nc-nd/4.0/).

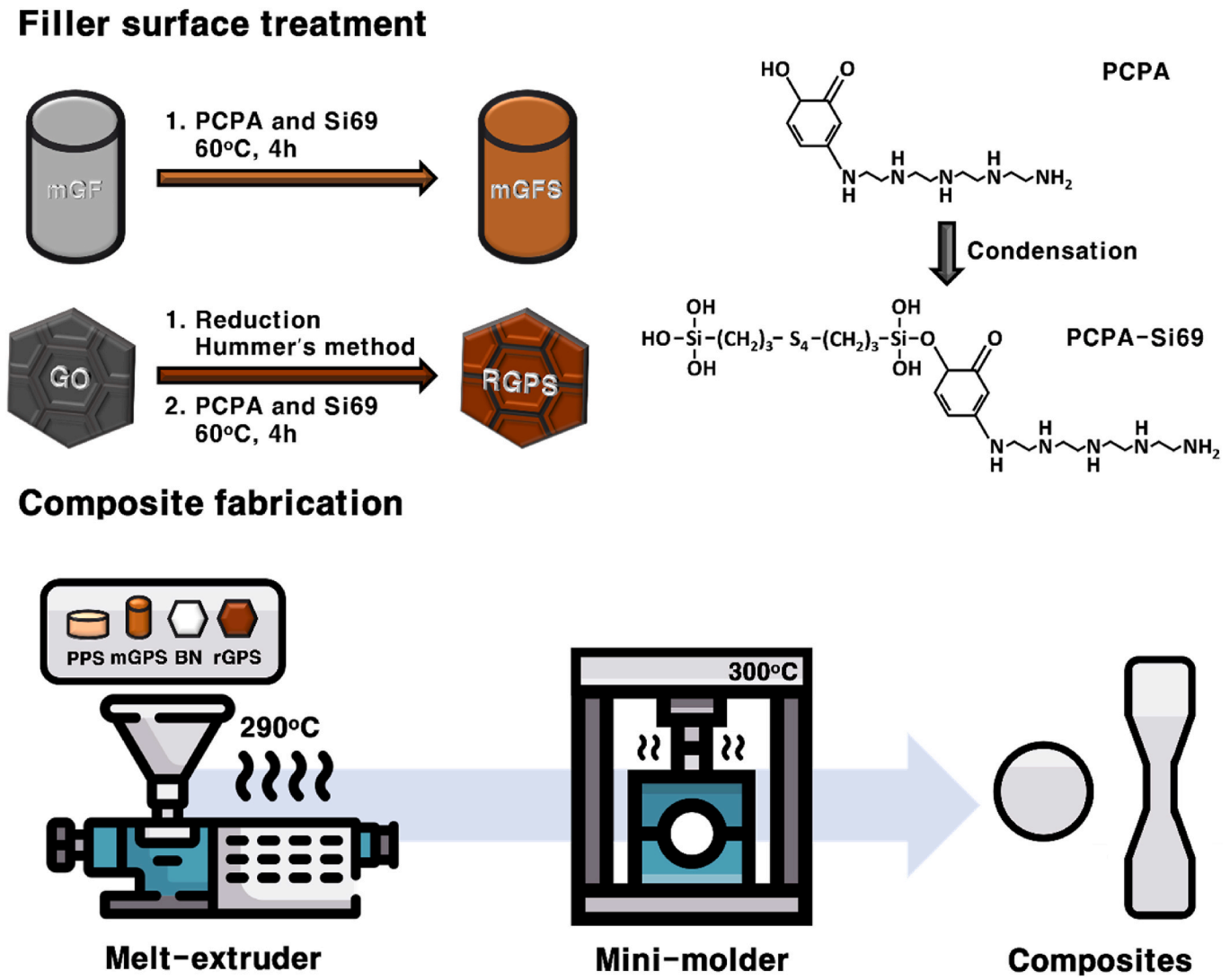


Fig. 1. Schematic of surface treatment and composite fabrication.

Table 1
Compositions of the matrices and composites.

Composite	Matrix			Composite			Total
	PPS	mGPS	Total	Matrix	BN	rGPS	
PPS	100 %	-	100 %	100 %	-	-	100.0
m10	90 %	10 %	100 %	100 %	-	-	100.0
m20	80 %	20 %	100 %	100 %	-	-	100.0
m30	70 %	30 %	100 %	100 %	-	-	100.0
m40	60 %	40 %	100 %	100 %	–	–	100.0
m40/B15	60 %	40 %	100 %	85 %	15 %	-	100.0
m40/B15/r3	60 %	40 %	100 %	82 %	15 %	3 %	100.0
m40/B15/r6	60 %	40 %	100 %	79 %	15 %	6 %	100.0
m40/B30	60 %	40 %	100 %	70 %	30 %	-	100.0
m40/B30/r3	60.00 %	40.00 %	100.00 %	67 %	30 %	3 %	100.0
m40/B30/r6	60.00 %	40.00 %	100.00 %	64 %	30 %	6 %	100.0

Graphene has recently become a focal point in research, primarily due to its outstanding thermal conductivity, reaching approximately 5300 $Wm^{-1}K^{-1}$ [36]. This remarkable property is realized through a two-dimensional pathway that facilitates both phononic and electronic heat transport [37,38]. For polymer composites, attaining the desired thermal conductivity hinges on two crucial factors: ensuring the even dispersion of fillers within the matrix and fostering robust interfacial adhesion [39,40]. However, despite the impressive thermal performance of graphene as a filler, the strong interactions among the sp2-conjugated carbon sheets can lead to aggregation within the polymer matrix. Moreover, the limited compatibility between graphene and the matrix results in weak interfacial interactions, creating acoustic phonon mismatches [41]. These mismatches impede heat transfer within the composite by introducing thermal boundary resistance [42]. Researchers have explored various approaches to overcome these limitations, with achieving functionalization through either chemisorption or physisorption of organic compounds using grafting or coating techniques being a common strategy [43,44].

M. Kim et al. prepared MgO@MoS_2 core–shell structure to fabricate composites. The PPS/MgO@MoS2/PA composites showed a filler ratio and thermal conductivity of 40 wt% and 4.07 W/m·K [45]. Seki et al. used carbon fiber and synthetic graphite hybrid filler to create blend of PPS and SPS composites. The PPS−SPS-30SG-10CF composites reached a filler ratio and thermal conductivity of 40 wt% and 4.17 W/m·K, respectively [46].

Silane coupling agents, known for forming strong connections between organic and inorganic materials, have played a crucial role in

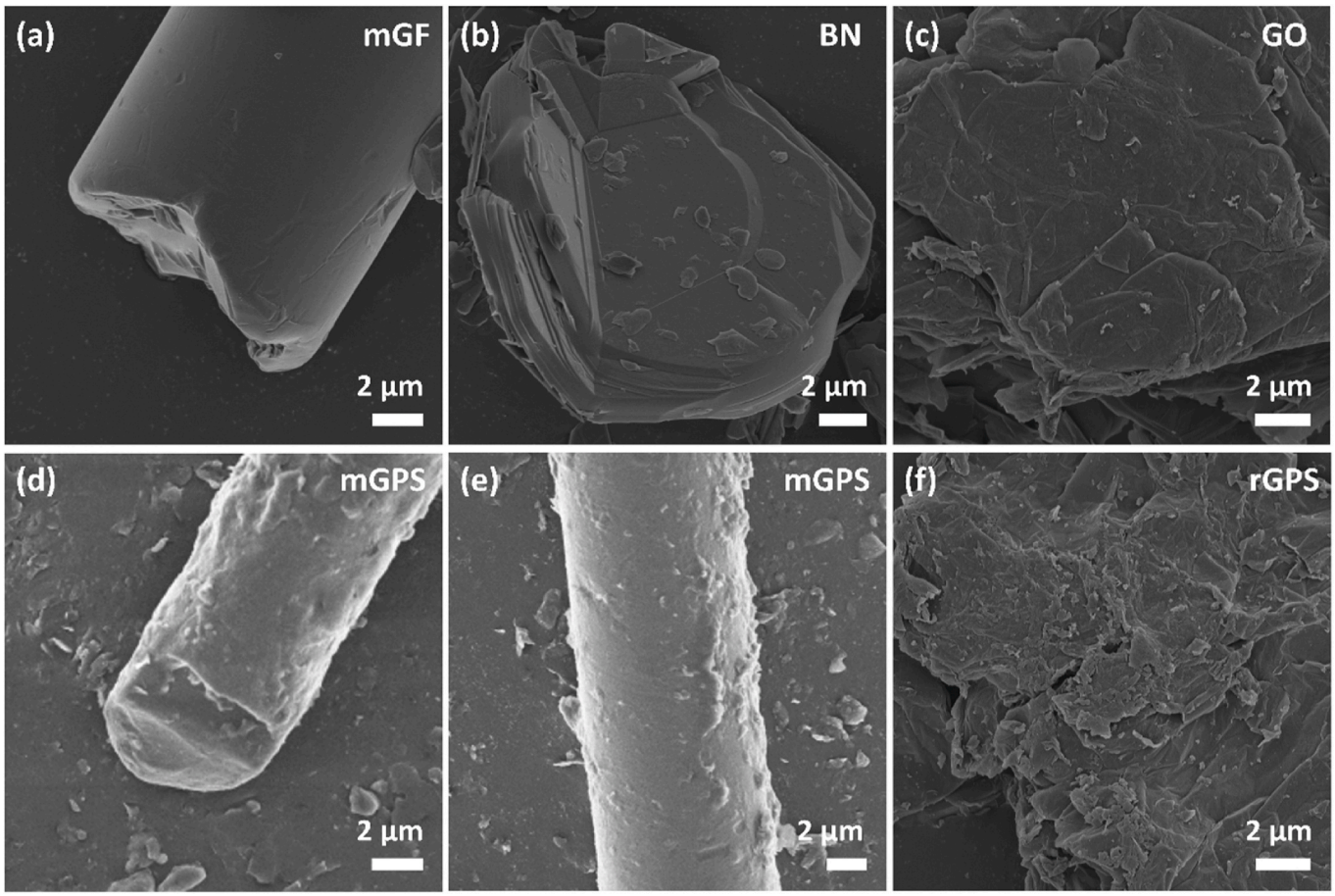


Fig. 2. FE-SEM images of (a) mGF, (b) BN, (c) GO, (d,e) mGPS, and (f) rGPS.

these endeavors [47,48]. Typically comprising silicon atoms with sulfide atoms; hydrolyzable components, often in the form of alkyl linkers; and an organofunctional group, these agents have proven invaluable [49,50]. In our experiment, we chose Bis[3-(triethoxysilyl)propyl] tetrasulfide (Si69) for this task.

Nevertheless, the substantial expense associated with dopamine creates a notable barrier to its extensive utilization in industrial applications [51]. Given the structural resemblance of both the catechol moiety and the amino-terminal group to dopamine, the potential to establish robust adhesion exists [52]. To provide a cost-effective alternative, this study opted for catechol and polyamine to synthesize PCPA in place of poly(dopamine). Consequently, the adoption of PCPA provided a cost-effective and straightforward approach, enabling the bonding of Si69 to the filler surface through polymerization at an appropriate pH. PCPA exhibits excellent adhesive performance and chemical reactivity for secondary reactions, making it useful for improving interfacial compatibility between fillers and the matrix. Si69, as a silane coupling agent, can enhance interfacial compatibility due to hydrogen bonding between the matrix and the hydroxyl groups on the silica surface [53,54].

In the research, composites were formulated by combining PPS with surface-treated mGF, raw BN, and GO fillers. The silane-treated mGFS and rGPS fillers were well dispersed when mixed with the PPS matrix. We analyzed the mechanical properties, thermal conductivity, and insulation of this composite according to the mixing ratio of BN and rGPS fillers.

2. Experimental

2.1. Materials

GO powder was obtained from Grapeneall Co., Republic of Korea. Hexagonal BN, boasting a purity of 99 % and an average diameter of 12 μm, was provided by Momentive Performance Materials Inc., USA. Milled glass fiber (mGF; average fiber length of 300 μm) was supplied from Fiber Man Co., Republic of Korea. PPS was provided by Lotte Chemical Co., Republic of Korea. Si69, polycatechol, and tetraethylenepentamine (TEPA) were acquired from Sigma Aldrich. Additionally, ethanol, distilled water, acetic acid, and hydroiodic acid needed for the experiment were supplied by Daejung Chemical Co., Republic of Korea.

2.2. Preparation of surface-treated GF

Fig. 1 shows the composite's surface treatment, reaction mechanism, and fabrication process. To prepare PCPA and conduct silane treatment, catechol, and PETA were mixed at a molar ratio of 3:1, whereas Si69 was incorporated at a weight ratio of 1:10 relative to mGF. Catechol, PETA, mGF, and Si69 were blended in 200 mL of distilled water. The solution was then stirred in an oil bath at 60 °C for 4 h at 500 rpm. The resulting material, having undergone PCPA and silane treatment, was subsequently filtered and dried in a vacuum oven at 70 °C for 48 h. This product, having undergone PCPA and silane treatment on mGF, was designated as mGPS.

2.3. Preparation of surface-treated GO

The process for reducing graphene oxide (GO) involved the use of

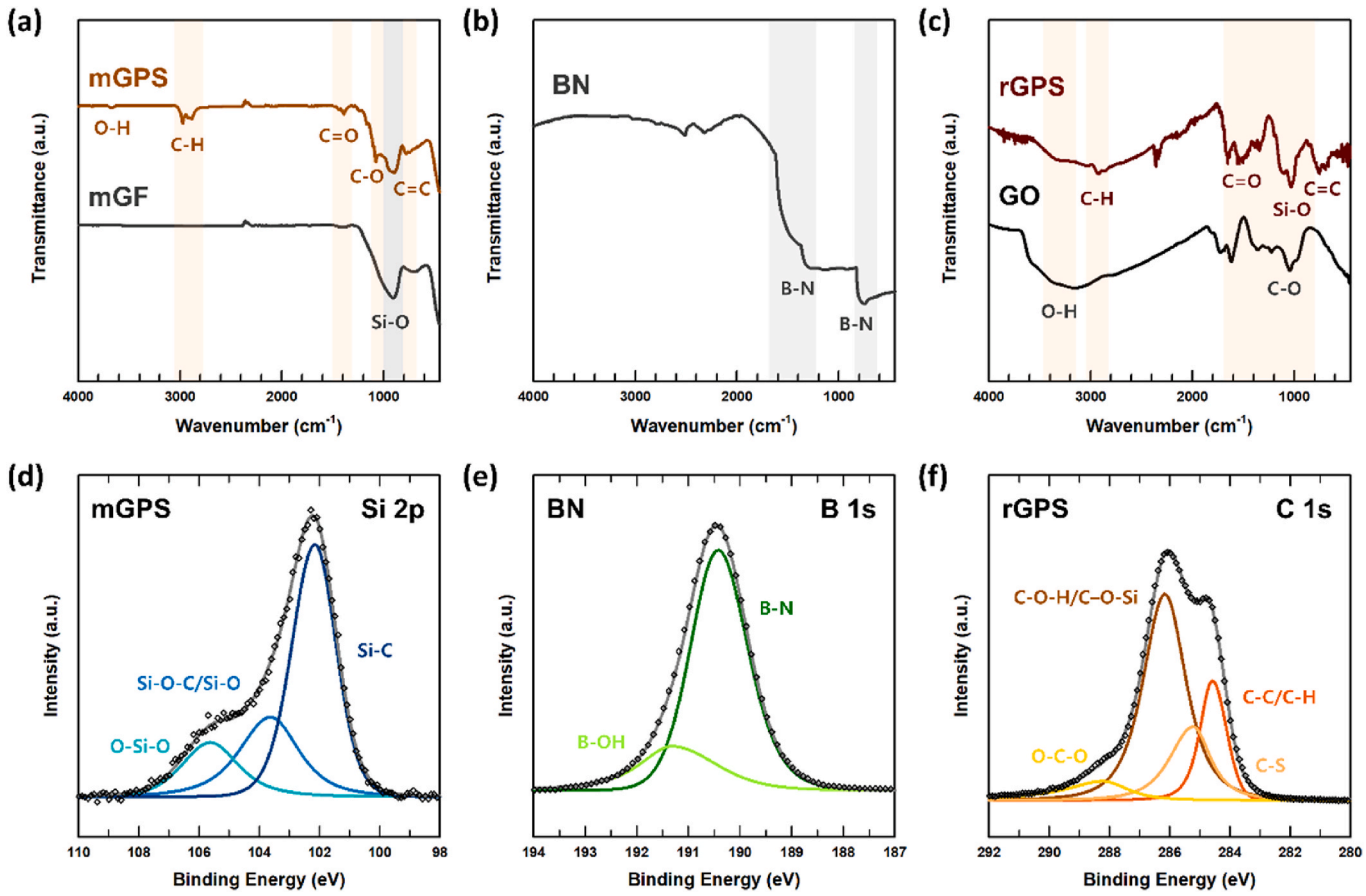


Fig. 3. FT-IR spectra (a) mGF and mGPS, (b) BN, and (c) GO and rGPS. XPS deconvolution of (d) Si 2p of mGPS, (e) B 1s of BN, and (f) C 1s of rGPS.

hydroiodic acid and acetic acid. The reduction solution was created by combining hydroiodic acid and acetic acid at a volume ratio of 3:1. Initially, 5 g of GO was dispersed in 200 mL of the reduction solution and stirred with a magnetic bar at 500 rpm for 24 h to form reduced graphene oxide (rGO). Afterward, the acidic rGO mixture was filtered thrice with di-water neutralizing its pH. The resulting rGO cakes from the filtration were subsequently dried in a vacuum oven at 70 °C for 48 h.

To prepare PCPA and conduct silane treatment, catechol, and PETA were mixed in a molar ratio of 3:1, whereas Si69 was incorporated in a weight ratio of 1:10 relative to rGO. Catechol, PETA, rGO, and Si69 were blended in 200 mL of distilled water. The solution was then stirred in an oil bath at 60 °C for 4 h at 500 rpm. The resulting material, having undergone PCPA and silane treatment, was subsequently filtered and dried in a vacuum oven at 70 °C for 48 h. This product, having undergone PCPA and silane treatment on rGO, was designated as rGPS.

2.4. Fabrication of the composites

Si69 and PCPA treated and untreated with mGF, BN, and GO were incorporated into PPS pellets using a twin-screw melt extruder (model BA-11, Bautek, Korea) operating at 290 °C. The extrudates were gathered and pelletized at 300 °C through injection molding (model BA-915, Bautek, Korea) to produce composites with diverse shapes. Subsequently, the mechanical and thermal properties of the resulting composites were thoroughly examined. The composition and their corresponding designations are listed in Table 1.

2.5. Characterization

The morphological features of the matrices, fillers, and composites were evaluated using a field-emission scanning electron microscope (FE-SEM; Sigma, Carl Zeiss). The platinum coating was done on the upper surface of the sample before imaging. This is because to use FE-SEM, the sample must be made conductive. The attenuated total reflection mode was used in Fourier-transform infrared spectroscopy (FT-IR; Spectrum One, PerkinElmer, USA), covering a wavelength range from 400 to 4000 cm^{-1}, and was employed to investigate the functional attributes of the matrix and surface modifications of the fillers. An ESCA 2000 X-ray photoelectron spectrometer (VG Microtech) was employed for X-ray photoelectron spectroscopy (XPS) to examine the surface characteristics of the BN and GO fillers. X-ray diffraction (XRD; New D8-Advance, Bruker-AXS) within a 2θ range of 10–80° confirmed the crystalline nature of both the matrix and fillers.

The thermal stability and degradation characteristics of the matrices, fillers, and composites were evaluated through thermogravimetric analysis (TGA; TGA 2050, TA Instruments) at a temperature range of 50–800 °C under a nitrogen atmosphere. Tensile strength and tensile strain of both matrices and composites were determined using a universal testing machine (UTM; 3344Q9465, Instron Co., Norwood, MA, USA) at a crosshead speed of 5 mm/min. Furthermore, dynamic mechanical analysis (DMA; PerkinElmer DMA 8000, PerkinElmer, Waltham, MA, USA) was performed to measure the storage modulus, loss modulus, and tan delta over a temperature range of 30–200 °C, with a heating rate of 3 °C/min and a frequency of 1 Hz.

The thermal conductivity was calculated using Equation (2) from the measured values:

$$K = \alpha \bullet \rho \bullet C_p \quad (2)$$

where K represents thermal conductivity, ρ is the density, α is the thermal diffusivity, and C_p is the heat capacity of the composite.

Thermal diffusivity, specific heat capacity, and bulk density were measured at room temperature using Laser Flash Analysis (LFA)

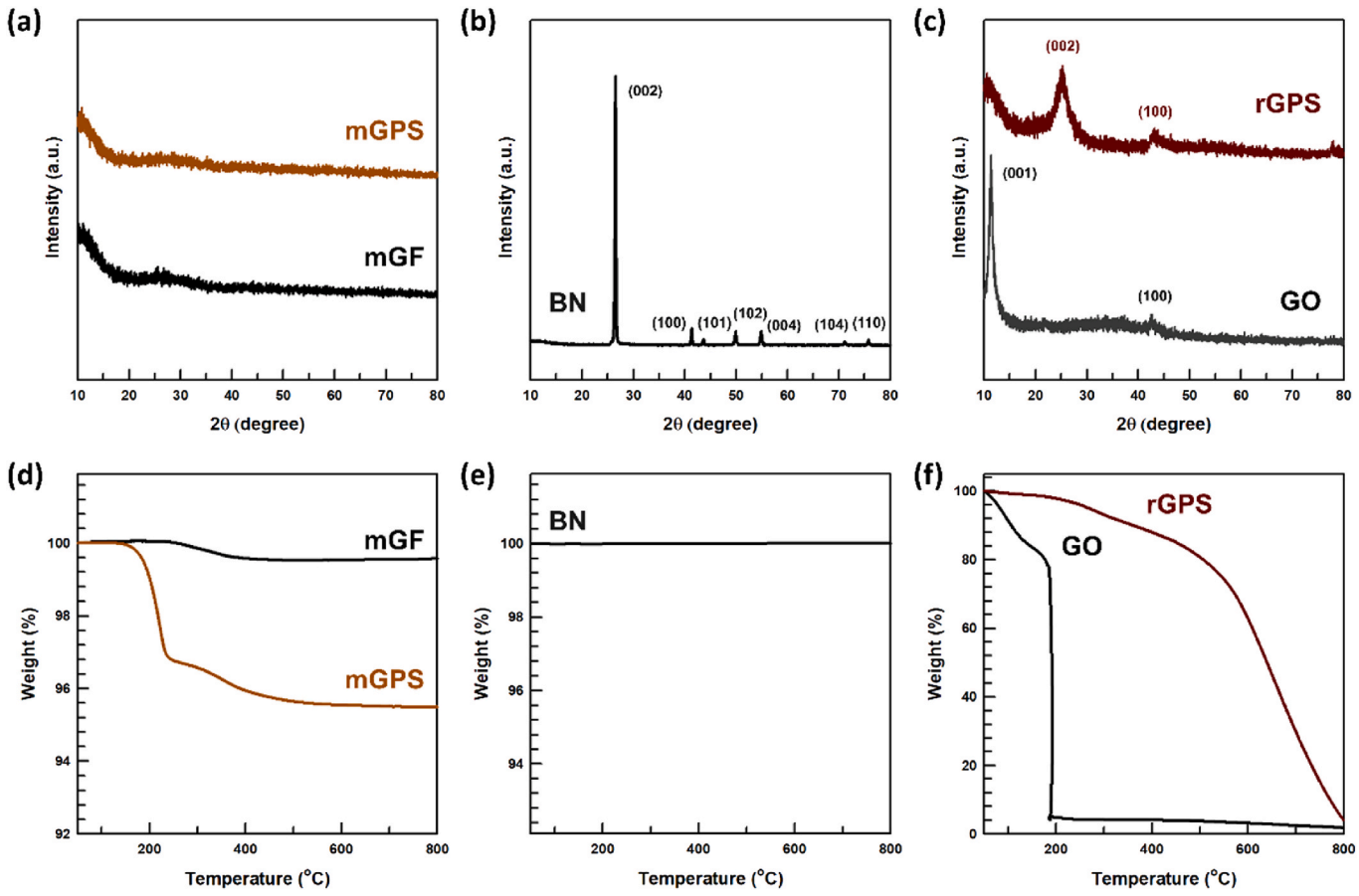


Fig. 4. XRD spectra of (a) mGF and mGPS, (b) BN, and (c) GO and rGPS. TGA curves of (d) BN, (e) mGF and mGPS, and (f) GO and rGPS.

(NanoFlash LFA 467, Netzsch Instruments Co., Selb, Germany), Differential Scanning Calorimetry (DSC-7, PerkinElmer Co.), and an Electromagnetic Balance (HR-250AZ, A&D Company Limited, Tokyo, Japan) that applies Archimedes' principle, respectively.

Finally, the thermal conductivity enhancement (TCE) was determined using Equation (3):

$$TCE = \frac{K - K_m}{K_m} \times 100\% \quad (3)$$

where K_m represents the thermal conductivity of the matrix.

3. Results and discussion

3.1. Filler characterization

Fig. 2 presents a comparative examination of the morphological characteristics of mGF, BN, and GO fillers, according to whether they underwent surface treatment. Raw fillers with clean surfaces are indicated in Fig. 2(a–c). However, Fig. 2 (d and e) shows the uneven surfaces of mGPS and rGPS. It indicates successful Si69 and PCPA grafting on the mGF and rGO surfaces after grafting the surface treatment agent. These effective surface modifications are illustrated by the morphological changes observed in the FE-SEM analysis.

Fig. 3 presents a comprehensive comparative analysis of the chemical properties of mGF, BN, and GO fillers in various states utilizing FT-IR and XPS spectra. Fig. 3(a) shows the raw mGF and mGPS. Significantly, both mGF and mGPG exhibit Si–O absorption peaks at approximately 900 cm^{-1}. Additionally, the FT-IR spectrum of mGPS reveals distinct peaks at 780, 1080, 1400, 2980, and 3680 cm^{-1}, corresponding to C=C, C–O, C=O, C–H, and O–H absorption. The FTIR spectrum of a raw BN is shown in Fig. 3(b). Raw BN exhibits B–N absorption peaks at approximately 765 and 1305 cm^{-1}. The FTIR spectra of raw GO and rGPS are depicted in Fig. 3(c). Raw GO exhibited peaks at approximately 1620 and 3400 cm^{-1} attributable to C–O and O–H stretching. The reduction and surface treatment process was confirmed by the FT-IR spectrum of rGPS, which exhibited noteworthy peaks at 765, 1035, 1550, 2925, and 3340 cm^{-1} corresponding to C=C, Si–O, C=O, C–H, and O–H stretching. These distinctive peaks in the GO and rGPS spectra provide clear evidence for the reduction and surface treatment of GO.

Furthermore, an XPS analysis was conducted to confirm the presence of PCPA and Si69 on the surfaces of the mGF and GO fillers as well as the state of BN. Fig. 3(d–f) depict the Si 2p deconvolutions of mGPS, B 1s deconvolutions of BN, and C 1s deconvolutions of rGPS, respectively. The deconvoluted Si 2p peaks in mGPS correspond to O–Si–O (105.6 eV), Si–O–C/Si–O (103.7 eV), and Si–C (102.2 eV) bonds. The deconvoluted B 1s peaks in BN filler are attributed to B–OH (191.2 eV) and B–N (190.4 eV). The rGPS filler exhibited peaks corresponding to O–C–O (288.3 eV), C–O–H/C–O–Si (286.2 eV), C–S (285.2 eV), and C–C/C–H (284.6 eV) bonds. These peaks provide evidence for the polymerization of PCPA and the presence of grafted silane molecules [55,56]. Notably, a slight shift in binding energy was observed due to different surface treatments. In summary, both FT-IR and XPS analyses confirmed the surface treatment applied to the fillers.

Fig. 4 presents a comparative analysis of the XRD spectra and TGA spectra of the fillers to assess their properties. In the XRD analysis of mGF and mGPS, the fillers exhibit no distinct peaks owing to the amorphous characteristics of mGF and PCPA. However, the XRD spectrum of BN displays distinctive patterns with peaks at approximately 26.46°, 41.23°, 43.67°, 49.88°, 54.84°, 71.18°, and 75.74°, corresponding to the (002), (100), (101), (102), (004), (104), and (110) planes. For GO, the XRD patterns reveal peaks at 11.37° and 42.59°,

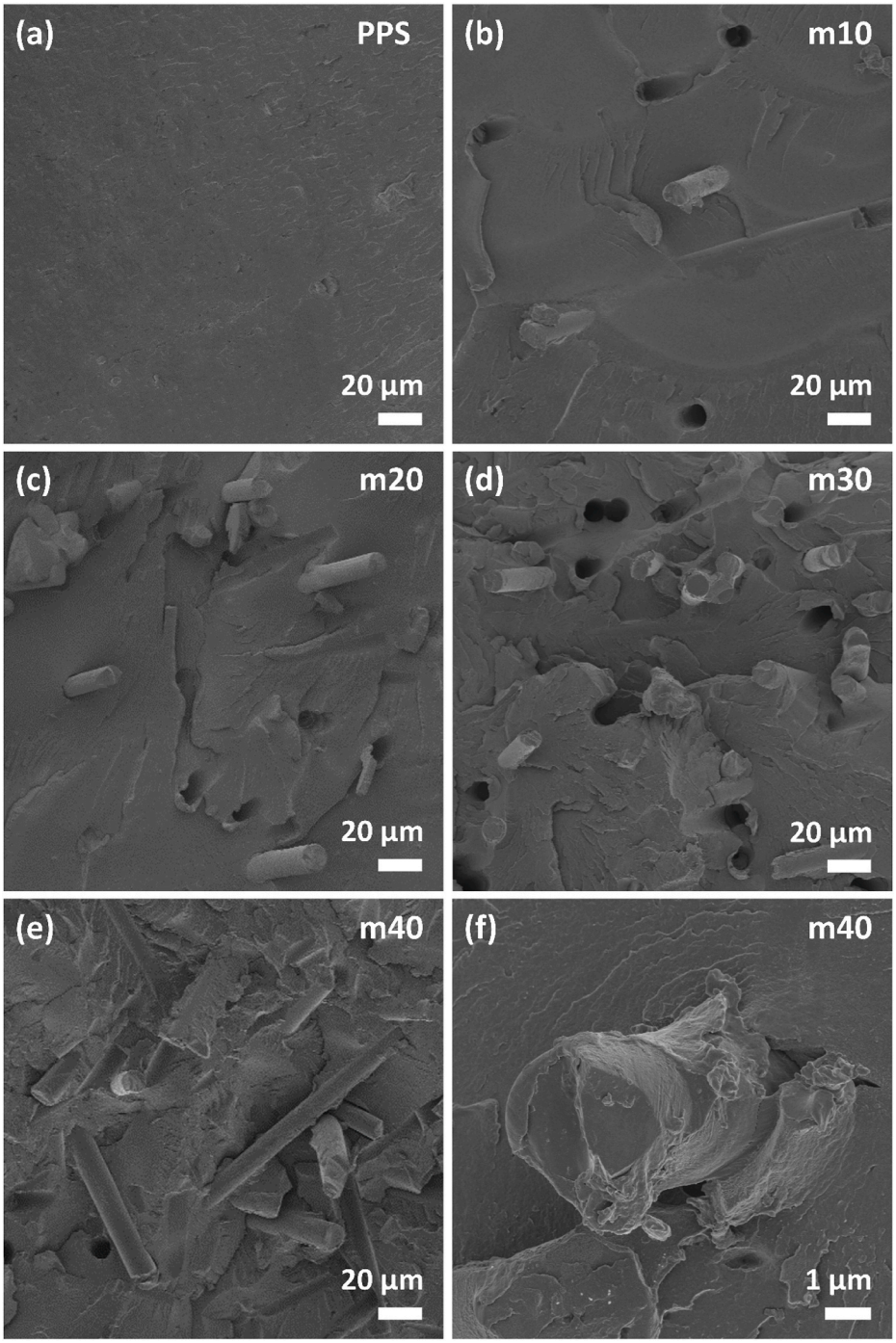


Fig. 5. Cross-sectional FE-SEM images of (a) PPS, (b) m10, (c) m20, (d) m30, (e) m40, and (f) mGPS in PPS.

corresponding to the (001) and (100) planes. The rGPS fillers, on the other hand, exhibited distinct peaks at 25.19° and 43.08°, corresponding to the (002) and (100) planes, attributable to the reduction procedure of GO. These XRD patterns demonstrate minor shifts for each filler, suggesting that the hydroxylation process and the attachment of surface-treatment agents had a modest impact on the crystallinity of the fillers [57,58].

To assess thermal stability and the composition of surface-treatment agents, the thermal degradation properties of the fillers are examined in Fig. 4(a–c). Raw mGF exhibits excellent thermal stability and, therefore, the ability to characterize the weight percentage of the grafted surface treatment agents in mGPS. The degraded weight percentage of the mGPS was 4.5 %, indicating that 4.5 wt% of the Si69 and PCPA were well attached to the surface of the filler. Raw BN displayed exceptional thermal stability, with a degradation temperature of 2973 °C. Comparatively, raw GO degraded was almost completely degraded at approximately 200 °C. However, rGPS exhibited enhanced thermal stability. The rGPS filler degraded slowly until the temperature reached 800 °C. Moreover, the GO reduction and PCPA polymerization with Si69 on the GO surface enhanced thermal stability [59,60]. This is because, after surface treatment of GO with PCPA and Si69, chemical bonds were formed. These bonds altered the thermal decomposition pathway, thereby increasing thermal stability [61].

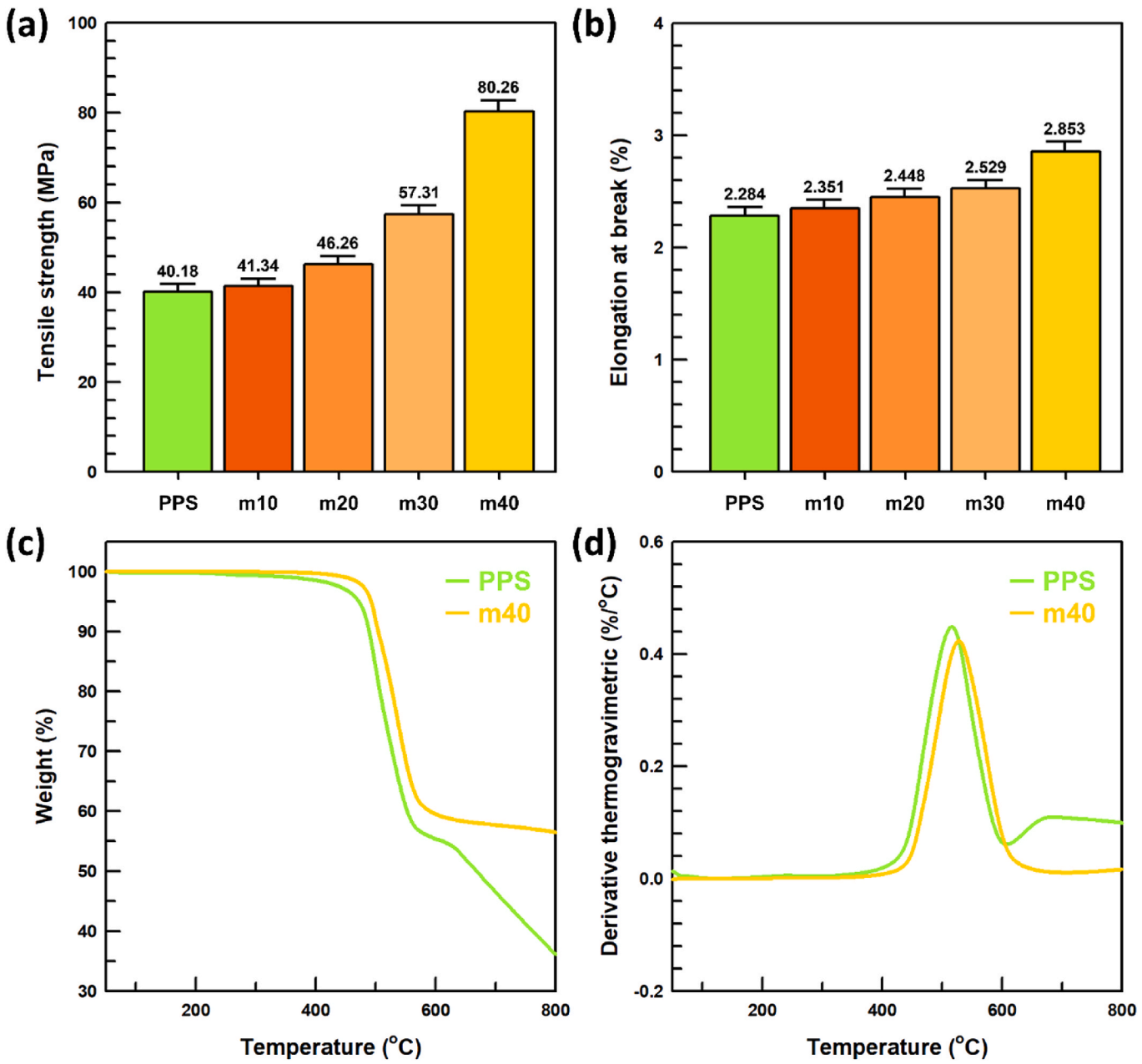


Fig. 6. (a) Tensile strengths, (b) elongation at break of the PPS and PPS/mGPS composites. (c) TGA and (d) dTG curves of PPS and m40.

3.2. Composite characterization

Fig. 5 presents cross-sectional FE-SEM images of the matrices with various contents of mGPS filler, ranging from raw PPS to m40, which contains 40 wt% of mGPS. To ensure a smooth surface for analysis, the samples were cryogenically frozen with liquid nitrogen and then fractured before FE-SEM imaging. As shown in Fig. 5, raw PPS exhibited clean and neat surfaces. However, with the increase in the content of mGPS filler, the matrices exhibited more cylindrical glass fibers as well as good filler dispersion. Fig. 5(e), depicting the m40 matrix, reveals that the mGPS fillers were not only vertically but also horizontally aligned in the matrix. As vertical injection molding was used to fabricate the matrices, the mGFS tended to be vertically aligned. However, an increase in the amount of mGFS led to both a vertical and horizontal distribution of the filler. Moreover, mGPS exhibited excellent interfacial interaction with PPS, as the filler was well-coated with PPS when it fractured.

Fig. 6(a and b) compare the mechanical properties among the matrices with various mGPS contents. In all ratios, the tensile strength increased as mGPS was added to PPS. As can be seen in the FE-SEM photos of m10, m20, and m30 in Fig. 5(b,c, and d), after vertical injection molding, mGFS was vertically aligned and the tensile strength also gradually increased to 41.34, 46.26, 57.31 MPa. On the other hand, at m40, it showed a sharply high tensile strength of 80.26 MPa, which is due to the increase in the ratio of mGFS in Fig. 5(e), the horizontally aligned mGFS increased the mechanical properties. The elongation at the break of the matrices exhibited a similar trend.

The adequate content of mGPS filler grants slight flexibility, as the filler has a good affinity to the PPS polymer. Importantly, the mGPS not only enhanced the dispersal of fillers in the matrix but also significantly improved the mechanical properties. When the content of mGFS exceeded 40 wt%, the amount of mGFS became too high compared to the PPS matrix, resulting in the inability to form a composite. Therefore, the m40 was chosen as a matrix for the fabricating composites.

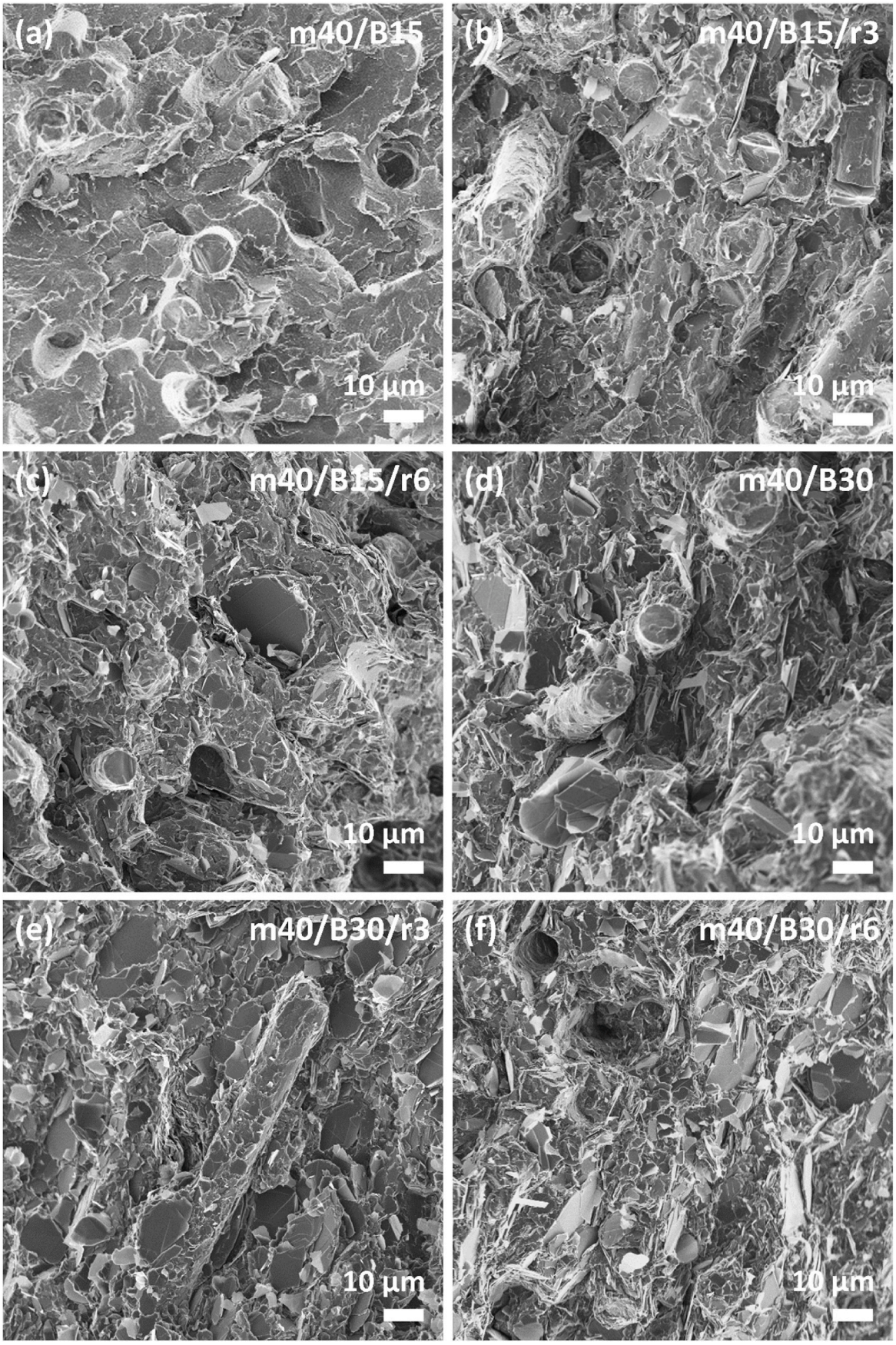


Fig. 7. Cross-sectional FE-SEM images of (a) m40/B15/r0, (b) m40/B15/r3, (c) m40/B15/r6, (d) m40/B30/r0, (e) m40/B30/r3, and (f) m40/B30/r6.

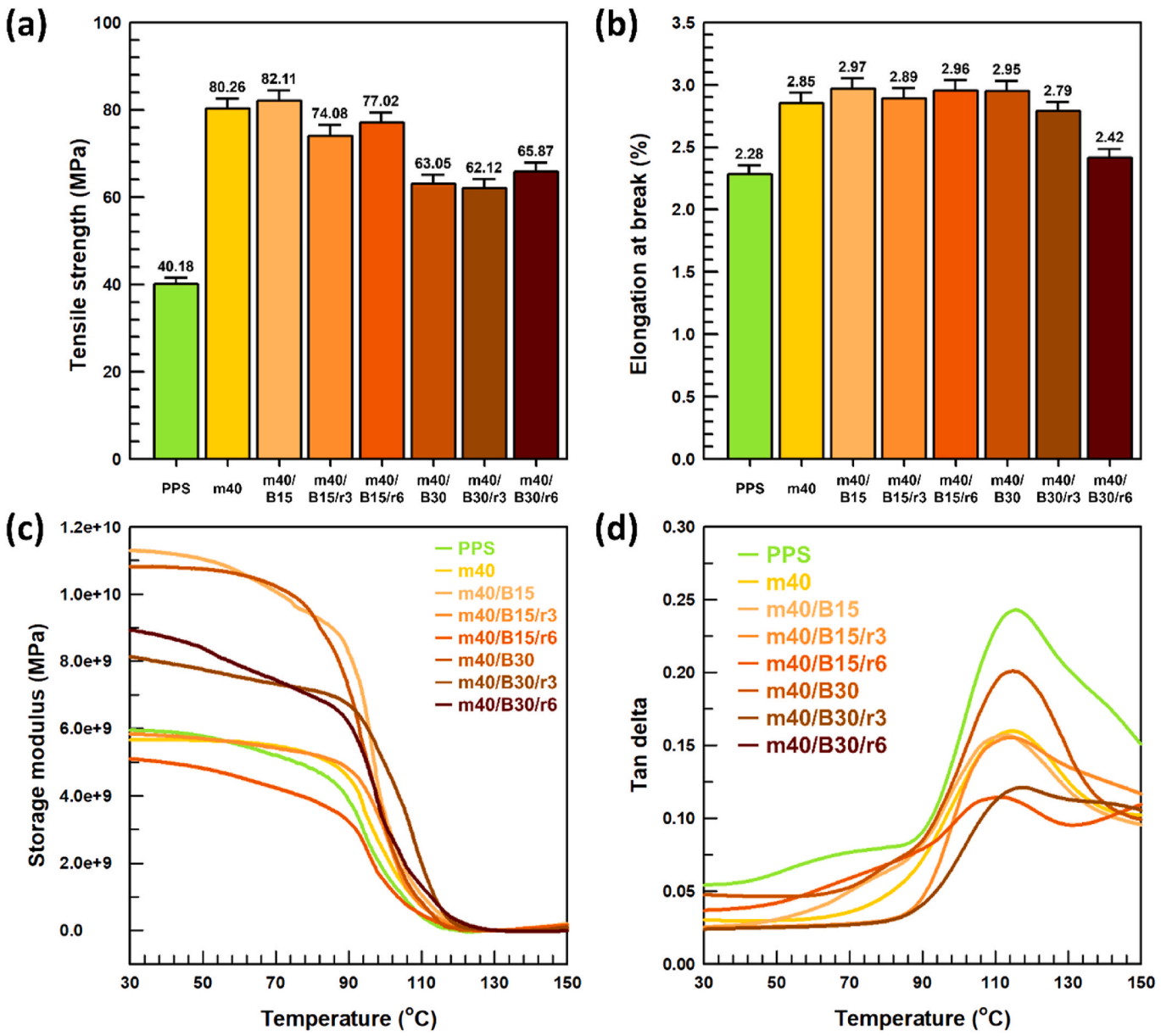


Fig. 8. (a) Tensile strengths, (b) elongation at break, (c) storage modulus, and (d) tan delta of the composites.

The TGA and dTG curves of PPS and m40 are compared in Fig. 6(c and d). The thermal stability of the m40 was enhanced through the incorporation of mGPS filler. Fig. 4 confirms that the thermally stable nature of mGPS increased the m40 matrix. Additionally, the successful attachment of mGPS filler on PPS owing to surface treatment led to an increase in mechanical strength and thermal stability.

Fig. 7 displays cross-sectional FE-SEM images of the composites. The mGPS and BN fillers were well dispersed in all composites. The hexagonal BN fillers and two-dimensional rGPS were attached to the cylindrical mGPS. The surface treatment of mGPS and rGPS played the increased affinity among fillers as well as with the PPS matrix. Therefore, a significant thermal conductivity enhancement is expected through the thermal pathway formed by hybrid fillers. Fig. S1 is the EDS elemental mapping image of the m40/B30/r6 composite. Through EDS elemental mapping, it can be confirmed that mGFS, rGPS, and BN are well dispersed in the PPS matrix.

Fig. 8 depicts a comparative analysis of the mechanical properties across different composites. The inclusion of BN fillers led to a gradual decline in mechanical strength. In contrast to the BN filler, when sufficient rGPS (6 wt%) was incorporated into the composites, the tensile strength increased. For instance, m40/B15/r6 and m40/B30/r6 demonstrated tensile strengths of 77.02 and 65.87, whereas those of m40/B15/r3 and m40/B30/r3 were 74.08 MPa and 62.12 MPa, respectively.

When the content of the filler BN increased from 15 wt% to 30 wt%, it was confirmed that the tensile strength decreased due to the excessive addition of the filler.

However, the integration of fillers did not significantly affect the elongation at break for the composites. Fig. 7 shows that the fillers and PPS were well mixed owing to the enhanced affinity following surface treatment, and the tensile strength remained similar to that of the m40 matrix. Consequently, the concurrent surface treatment of fillers using Si69 and PCPA not only improved the dispersion of fillers in the matrix but also significantly improved the mechanical properties.

In Fig. 8(c), an increasing concentration of BN filler within the composites led to an increase in storage modulus. This behavior can be attributed to the addition of BN, which hindered the molecular chain mobility and movement within the matrix. In contrast, when the carbon

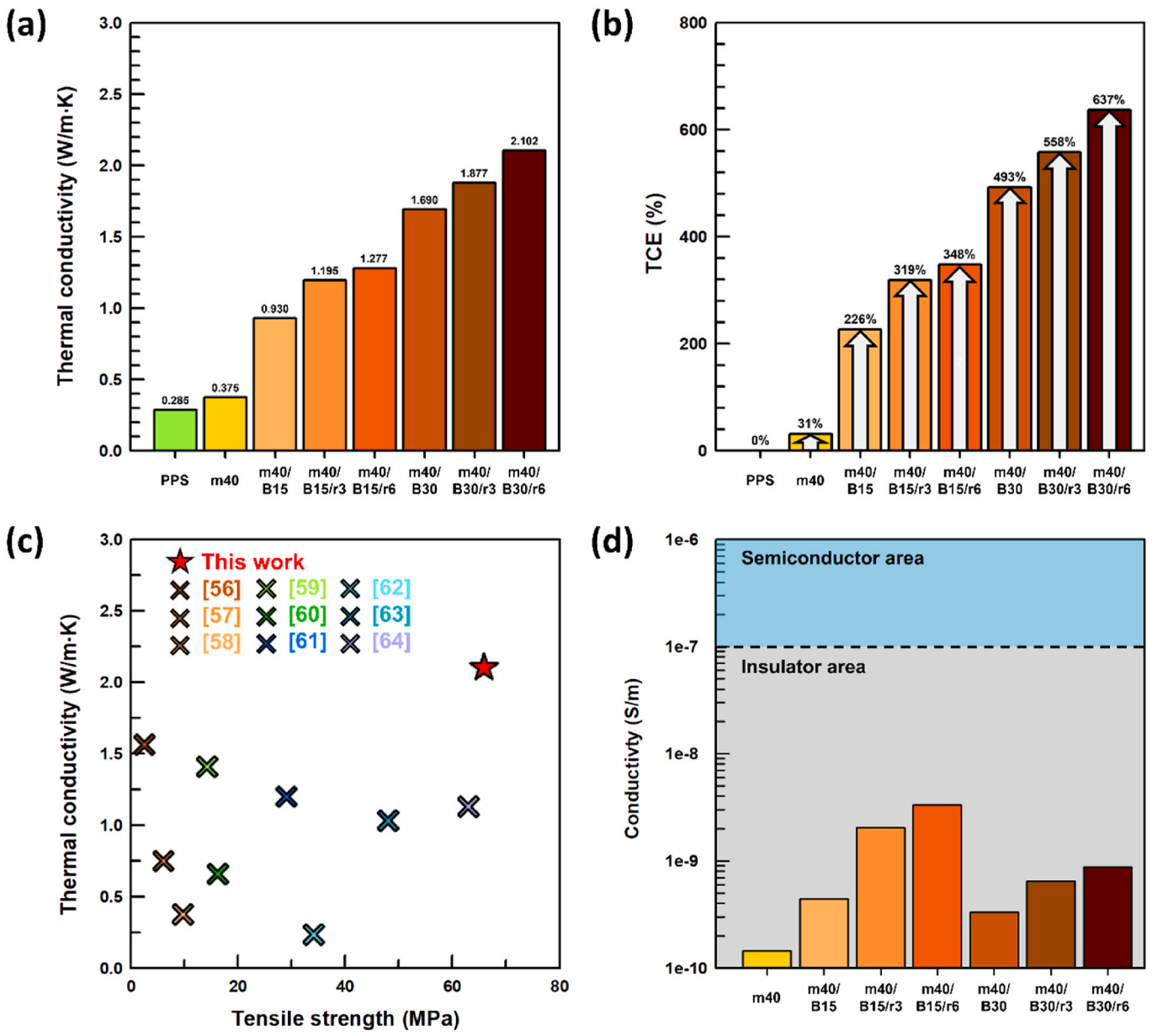


Fig. 9. (a) Thermal conductivities and (b) Thermal conductivity enhancement of the composites. (c) Thermal conductivity versus tensile strength of the composite compared with those in the literature [66–74]. (d) Electrical insulation of the composites.

filler rGPS content increased, the storage modulus decreased. This is because well-dispersed rGPS, which is compatible with the matrix, softened the stiffness between the BN fillers that hindered the matrix's molecular chain mobility and movement [62,63].

Similarly in the tan δ curve of Fig. 8(d), as the content of fillers increases, the tan δ curve corresponding to the glass transition temperature peak tends to shift in the high-temperature direction. As the content of rGPS grafted with Si69 and PCPA increases, the mobility and movement of the matrix's molecular chain are restricted due to hydrogen bonding with PPS and mGPS [64,65].

Consistent with the observations from the UTM results, the DMA results confirm that the inclusion of various fillers deteriorated the mechanical properties.

Fig. 9(a–d) compares the matrix and various composites' thermal conductivity and thermal conductivity enhancement (TCE). Thermal conductivities for the matrix and composites PPS, m40, m40/B15, m40/B15/r3, m40/B15/r6, m40/B30, m40/B30/r3, and m40/B30/r6 were measured at 0.285, 0.375, 0.930, 1.195, 1.277, 1.690, 1.877, and 2.102 $Wm^{-1}K^{-1}$, respectively. Notably, m40/B30/r6 exhibited the most substantial enhancement, demonstrating an impressive 637 % increase in thermal conductivity. As shown in the FE-SEM images of Fig. 5(e) and 7 (e and f) and S2, BN and rGPS, which are fillers with high thermal conductivity, were arranged following the mGPS fiber, thereby forming a heat transfer path. Moreover, the successful surface treatment and well-dispers of these hybrid fillers led to an overall enhancement in the thermal conductivity of the composites.

The incorporation of 30 wt% BN and 6 wt% rGPS hybrid fillers with surface treatment produced the highest TCE among the various composites.

Fig. 9(c) compares the thermal conductivity and elongation at break values obtained in this study and those of flexible polymer composites reported in various studies. The electrical insulation properties were also assessed by measuring the electrical conductivities of both the matrix and composites, as depicted in Fig. 9(d). The addition of BN and the implementation of surface treatment contributed to the enhancement of the electrical insulation properties. Notably, all the composites

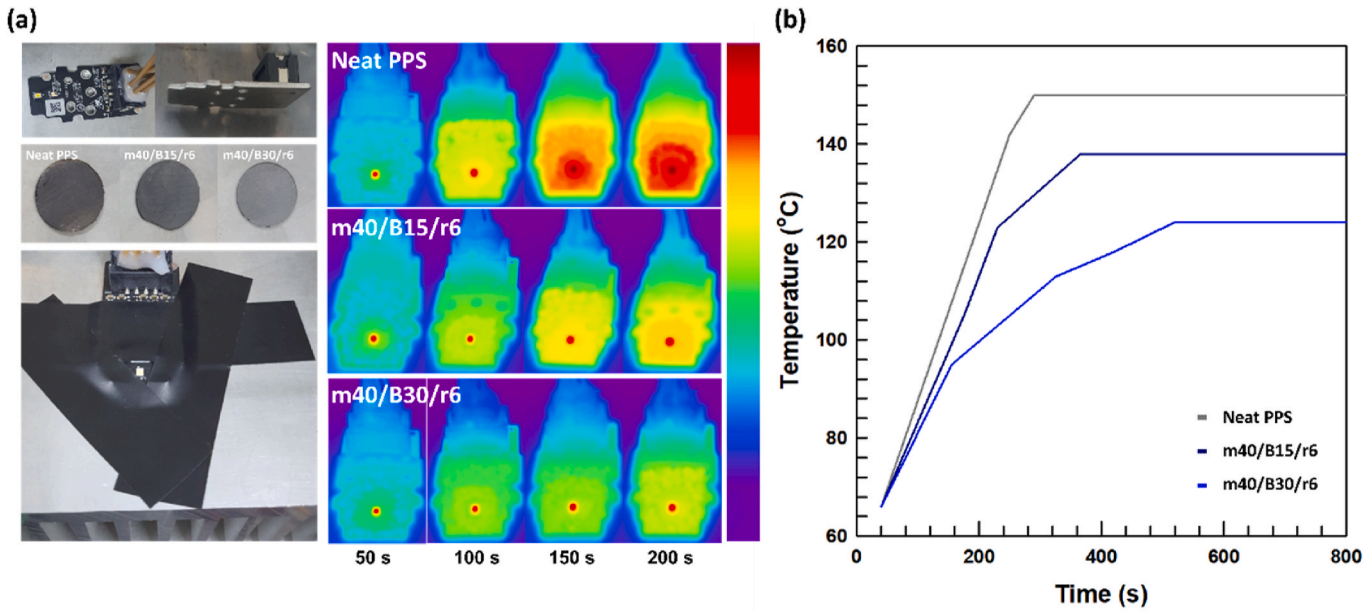


Fig. 10. Applications in thermal management, thermal images of a light-emitting diode (LED) lamp 7(a), and the temperature variation of the LED lamp over time (b).

demonstrated commendable electrical insulation characteristics.

Furthermore, the heat-dissipation capabilities of selected film samples were investigated using an infrared camera. This analysis entailed the acquisition of sample images as a light-emitting diode (LED) generated heat, which was subsequently passed to the heat sink. The surface temperature of the LED lamp was documented using an infrared camera, as depicted in Fig. 10(a). A sequence of thermal images demonstrated that the exterior temperature of the LED lamp, when equipped with the neat PPS and m40/B15/r3 composite was higher than that with the m40/B30/r6 composite, indicating the outstanding heat-dispersion ability of the m40/B30/r6 composite. As depicted in Fig. 10(b), the LED lamp with the neat PPS maintained a temperature of 150 °C for 280 s, the m40/B15/r3 composite maintained a temperature of 138 °C for 410 s, and the m40/B30/r6 composite maintained a temperature of 124 °C for 640 s. The m40/B30/r6 composite exhibited a mean temperature variation of 26 °C compared to the neat PPS, and the m40/B15/r3 composite exhibited a difference of 14 °C. This is because the horizontal distribution of mGFS led to the alignment of fillers rGPS and BN, and the treatments with PCPA and Si69 enhanced the interfacial compatibility between the filler and the matrix. These fillers were crucial in forming heat transmission pathways, which facilitated efficient heat dissipation.

4. Conclusion

PPS has advantages such as high-temperature resistance, chemical resistance, and flame retardancy in the field of engineering plastics. However, it has the disadvantage of lower thermal conductivity compared to other engineering plastics. This study focuses on developing highly thermally conductive composites by integrating a hybrid filler composed of mGF, BN, and GO into PPS. The resulting surface-treated hybrid composite exhibited an impressive thermal conductivity of 2.102 Wm-1K-1 and a tensile strength of 65.87 MPa, representing remarkable increases of 637 % and 63.94 %, respectively, compared to the base matrix. The improvement in high thermal conductivity and mechanical properties was achieved for the following two reasons:

(1) The surface-treated mGPS was mixed into the PPS matrix and evenly dispersed. With the aid of mGPS, the plate-shaped structures of rGPS and BN were evenly dispersed and arranged vertically, forming a heat transfer path, resulting in the m40/B30/r6 composite achieving high thermal conductivity.
(2) We created mGFS and rGPS fillers by performing silane surface treatment on mGF and GO using Si69 and PCPA. The surface treatment enhanced the compatibility between the fillers and the matrix, contributing to improved thermal conductivity and mechanical properties.

In conjunction with the straightforward melt extrusion process involving PCPA and Si69, this provides a quick and convenient solution to the challenges associated with mechanical strength and heat dissipation in EVs and electronic devices.

CRediT authorship contribution statement

Youngsung Cho: Writing – review & editing, Writing – original draft, Visualization, Software, Methodology, Investigation, Formal analysis, Data curation, Conceptualization. **Jangwoo Cho:** Writing – review & editing, Writing – original draft, Visualization, Software, Investigation, Formal analysis, Data curation. **Jooheon Kim:** Validation, Supervision, Resources, Project administration, Funding acquisition.

Declaration of competing interest

The authors declare that they have no known competing financial interests or personal relationships that could have appeared to influence the work reported in this paper.

Acknowledgements

This research was supported by the Industrial Technology Innovation Program (20011165) funded by the Ministry of Trade, Industry & Energy (MOTIE, Korea) and supported by the Human Resources Development (No. 20214000000280) of the Korea Institute of Energy Technology Evaluation and Planning (KETEP) grant funded by the Korea government Ministry of Trade, Industry and Energy.

Appendix A. Supplementary data

Supplementary data to this article can be found online at https://doi.org/10.1016/j.polymertesting.2024.108633.

Data availability

The data that has been used is confidential.

References

[1] Z. Liu, T. Sun, Y. Yu, P. Ke, Z. Deng, C. Lu, et al., Near-real-time carbon emission accounting technology toward carbon neutrality, Engineering 14 (2022) 44–51, https://doi.org/10.1016/j.eng.2021.12.019.

[2] N. Sulaiman, M.A. Hannan, A. Mohamed, E.H. Majlan, W.R. Wan Daud, A review on energy management system for fuel cell hybrid electric vehicle: issues and challenges, Renew. Sustain. Energy Rev. 52 (2015) 802–814, https://doi.org/10.1016/j.rser.2015.07.132.

[3] M.K. Hasan, M. Mahmud, A.K.M. Ahasan Habib, S.M.A. Motakabber, S. Islam, Review of electric vehicle energy storage and management system: standards, issues, and challenges, J. Energy Storage 41 (2021), https://doi.org/10.1016/j.est.2021.102940.

[4] W. Zhang, J. Xu, Advanced lightweight materials for Automobiles: a review, Mater. Des. 221 (2022), https://doi.org/10.1016/j.matdes.2022.110994.

[5] M.K. Gupta, V. Singhal, Review on materials for making lightweight vehicles, Mater. Today Proc. 56 (2022) 868–872, https://doi.org/10.1016/j.matpr.2022.02.517.

[6] M. Kim, J. Kim, Enhancement of the flame retardant properties of PPS-based composites via the addition of melamine-coated CaAl-LDH fire-retardant filler, Eur. Polym. J. 201 (2023) 112584, https://doi.org/10.1016/j.eurpolymj.2023.112584.

[7] P. Kulkarni, V. Ravekar, P. Rama Rao, S. Waigokar, S. Hingankar, Recycling of waste HDPE and PP plastic in preparation of plastic brick and its mechanical properties, Cleaner Mater. 5 (2022), https://doi.org/10.1016/j.clema.2022.100113.

[8] A.A. Karanastasis, V. Safin, L.M. Pitet, Bio-Based upcycling of poly(ethylene terephthalate) waste for the preparation of high-performance thermoplastic copolyesters, Macromolecules 55 (2022) 1042–1049, https://doi.org/10.1021/acs.macromol.1c02338.

[9] S. Lee, Y.R. Lee, S.J. Kim, J.S. Lee, K. Min, Recent advances and challenges in the biotechnological upcycling of plastic wastes for constructing a circular bioeconomy, Chem. Eng. J. 454 (2023), https://doi.org/10.1016/j.cej.2022.140470.

[10] T. Aziz, F. Haq, A. Farid, M. Kiran, S. Faisal, A. Ullah, et al., Challenges associated with cellulose composite material: facet engineering and prospective, Environ. Res. 223 (2023), https://doi.org/10.1016/j.envres.2023.115429.

[11] R. Petrény, L. Mészáros, Moisture dependent tensile and creep behaviour of multi-wall carbon nanotube and carbon fibre reinforced, injection moulded polyamide 6 matrix multi-scale composites, J. Mater. Res. Technol. 16 (2022) 689–699, https://doi.org/10.1016/j.jmrt.2021.12.030.

[12] L. Tang, S. Shao, A. Wang, C. Tian, F. Luo, J. Li, et al., Influence of fluorocarbon side chain on microphase separation and chemical stability of silicon-containing polycarbonate urethane, Polymer (Guildf) 242 (2022), https://doi.org/10.1016/j.polymer.2022.124538.

[13] U. Abid, G. Sun, Y.H.V. Soong, A. Williams, A.C. Chang, C. Ayafor, et al., Evaluation of enzymatic depolymerization of PET, PTT, and PBT polyesters, Biochem. Eng. J. 199 (2023), https://doi.org/10.1016/j.bej.2023.109074.

[14] L. Zhang, T. Chen, H. Xu, X. Liu, J. Zhang, R. Chai, Simultaneously enhanced flame retardancy and smoke suppression properties of flexible polyvinyl chloride with the incorporation of modified Mg(OH)2 and Sb2O3, Mater. Today Commun. 34 (2023), https://doi.org/10.1016/j.mtcomm.2023.105448.

[15] L.C. Jia, Y.F. Jin, J.W. Ren, L.H. Zhao, D.X. Yan, Z.M. Li, Highly thermally conductive liquid metal-based composites with superior thermostability for thermal management, J. Mater. Chem. C. Mater. 9 (2021) 2904–2911, https://doi.org/10.1039/d0tc05493c.

[16] Y.K. Li, W.J. Li, Z.X. Wang, P.Y. Du, L. Xu, L.C. Jia, et al., High-efficiency electromagnetic interference shielding and thermal management of high-graphene nanoplate-loaded composites enabled by polymer-infiltrated technique, Carbon N Y 211 (2023), https://doi.org/10.1016/j.carbon.2023.118096.

[17] Z. Sun, B. Wang, Y. Yao, S. Wang, W. Zhang, H. Zhang, Thermo-mechanical simulation of friction spot joining of aluminum alloys to short glass fiber-reinforced PPS, CIRP J. Manuf. Sci. Technol. 43 (2023) 30–41, https://doi.org/10.1016/j.cirpj.2023.03.001.

[18] S. Kumagai, M. Sato, C. Ma, Y. Nakai, T. Kameda, Y. Saito, et al., A comprehensive study into the thermo-oxidative degradation of sulfur-based engineering plastics, J. Anal. Appl. Pyrolysis 168 (2022), https://doi.org/10.1016/j.jaap.2022.105754.

[19] S. Ahn, C. Park, S. Park, J.H. Choi, Y.S. Kim, Y. Yoo, Effective flow modifiers for high-filled poly(phenylene sulfide) composites based on chemical structure similarity, Compos. Sci. Technol. 230 (2022), https://doi.org/10.1016/j.compscitech.2022.109721.

[20] Y. Gao, X. Zhou, M. Zhang, L. Lyu, Z. Li, Polyphenylene sulfide-based membranes: recent progress and future perspectives, Membranes (Basel) 12 (2022), https://doi.org/10.3390/membranes12100924.

[21] C. Shu, H.Y. Zhao, S. Zhao, W. Deng, P. Min, X.H. Lu, et al., Highly thermally conductive phase change composites with anisotropic graphene/cellulose nanofiber hybrid aerogels for efficient temperature regulation and solar-thermal-electric energy conversion applications, Compos. B Eng. 248 (2023), https://doi.org/10.1016/j.compositesb.2022.110367.

[22] X. Tan, T.H. Liu, W. Zhou, Q. Yuan, J. Ying, Q. Yan, et al., Enhanced electromagnetic shielding and thermal conductive properties of polyolefin composites with a Ti3C2TxMXene/graphene framework connected by a hydrogen-bonded interface, ACS Nano 16 (2022) 9254–9266, https://doi.org/10.1021/acsnano.2c01716.

[23] D. Liu, H. Chi, C. Ma, M. Song, P. Zhang, P. Dai, Improving in-plane and out-of-plane thermal conductivity of polyimide/boron nitride film with reduced graphene oxide by a moving magnetic field induction, Compos. Sci. Technol. 220 (2022), https://doi.org/10.1016/j.compscitech.2022.109292.

[24] N. Zhang, Y. Mao, S. Wu, W. Xu, Effects of the ball milling process on the particle size of graphene oxide and its application in enhancing the thermal conductivity of wood, Forests 13 (2022), https://doi.org/10.3390/f13081325.

[25] B. Liu, N. Vu-Bac, X. Zhuang, X. Fu, T. Rabczuk, Stochastic full-range multiscale modeling of thermal conductivity of Polymeric carbon nanotubes composites: a machine learning approach, Compos. Struct. 289 (2022), https://doi.org/10.1016/j.compstruct.2022.115393.

[26] Y. Cho, S. Han, J. Kim, Improved thermal, dielectric, and mechanical properties of acrylate composites with diethylene glycol and silane-treated ternary hybrid fillers via three-dimensional vat photopolymerization, Mater. Chem. Phys. 309 (2023), https://doi.org/10.1016/j.matchemphys.2023.128360.

[27] Y. Chen, H. Zhang, J. Chen, Y. Guo, P. Jiang, F. Gao, et al., Thermally conductive but electrically insulating polybenzazole nanofiber/boron nitride nanosheets nanocomposite paper for heat dissipation of 5G base stations and transformers, ACS Nano 16 (2022) 14323–14333, https://doi.org/10.1021/acsnano.2c04534.

[28] Y. Cho, J. Kim, Enhanced thermal and mechanical properties of 3D-printed PEG containing acrylate composite with surface-treated BN via digital light processing, Polym. Test. 118 (2023), https://doi.org/10.1016/j.polymertesting.2022.107898.

[29] Y. Cho, J. Kim, Effects of two silane surface modifications with different functional groups on the thermal conductivity and mechanical properties of UV-cured composites with high ceramic filler loading, Ceram. Int. 48 (2022) 32001–32008, https://doi.org/10.1016/j.ceramint.2022.07.137.

[30] V. Guerra, C. Wan, T. McNally, Thermal conductivity of 2D nano-structured boron nitride (BN) and its composites with polymers, Prog. Mater. Sci. 100 (2019) 170–186, https://doi.org/10.1016/j.pmatsci.2018.10.002.

[31] M. Li, M. Wang, X. Hou, Z. Zhan, H. Wang, H. Fu, et al., Highly thermal conductive and electrical insulating polymer composites with boron nitride, Compos. B Eng. 184 (2020), https://doi.org/10.1016/j.compositesb.2020.107746.

[32] Z. Wang, G. Meng, L. Wang, L. Tian, S. Chen, G. Wu, et al., Simultaneously enhanced dielectric properties and through-plane thermal conductivity of epoxy composites with alumina and boron nitride nanosheets, Sci. Rep. 11 (2021), https://doi.org/10.1038/s41598-021-81925-x.

[33] L.C. Jia, Z.X. Wang, L. Wang, J.F. Zeng, P.Y. Du, Y.F. Yue, et al., Self-standing boron nitride bulks enabled by liquid metals for thermal management, Mater. Horiz. 10 (2023) 5656–5665, https://doi.org/10.1039/d3mh01359f.

[34] F.W. Huang, Q.C. Yang, L.C. Jia, D.X. Yan, Z.M. Li, Aramid nanofiber assisted preparation of self-standing liquid metal-based films for ultrahigh electromagnetic interference shielding, Chem. Eng. J. 426 (2021), https://doi.org/10.1016/j.cej.2021.131288.

[35] L.C. Jia, Y.F. Yue, J.F. Zeng, Z.X. Wang, R.P. Nie, L. Xu, et al., A review on thermal and electrical behaviours of liquid metal-based polymer composites, J. Mater. Chem. C. Mater. 11 (2023) 12807–12827, https://doi.org/10.1039/d3tc02560h.

[36] T. Wu, Y. Xu, H. Wang, Z. Sun, L. Zou, Efficient and inexpensive preparation of graphene laminated film with ultrahigh thermal conductivity, Carbon N Y 171 (2021) 639–645, https://doi.org/10.1016/j.carbon.2020.09.039.

[37] A.A. Balandin, Phononics of graphene and related materials, ACS Nano 14 (2020) 5170–5178, https://doi.org/10.1021/acsnano.0c02718.

[38] W. Zheng, B. Huang, Y.K. Koh, Ultralow thermal conductivity and thermal diffusivity of graphene/metal heterostructures through scarcity of low-energy modes in graphene, ACS Appl. Mater. Interfaces 12 (2020) 9572–9579, https://doi.org/10.1021/acsami.9b18290.

[39] C.H. Lee, A. Khalina, S.H. Lee, Importance of interfacial adhesion condition on characterization of plant-fiber-reinforced polymer composites: a review, Polymers (Basel) 13 (2021) 1–22, https://doi.org/10.3390/polym13030438.

[40] B. Zhang, L. Jia, M. Tian, N. Ning, L. Zhang, W. Wang, Surface and interface modification of aramid fiber and its reinforcement for polymer composites: a review, Eur. Polym. J. 147 (2021), https://doi.org/10.1016/j.eurpolymj.2021.110352.

[41] L. Zhao, Z. Chen, J. Ren, L. Yang, Y. Li, Z. Wang, et al., Synchronously improved thermal conductivity and dielectric constant for epoxy composites by introducing functionalized silicon carbide nanoparticles and boron nitride microspheres, J. Colloid Interface Sci. 627 (2022) 205–214, https://doi.org/10.1016/j.jcis.2022.07.058.

[42] H. Yu, P. Guo, M. Qin, G. Han, L. Chen, Y. Feng, et al., Highly thermally conductive polymer composite enhanced by two-level adjustable boron nitride network with leaf venation structure, Compos. Sci. Technol. 222 (2022), https://doi.org/10.1016/j.compscitech.2022.109406.

[43] K. Ruan, X. Shi, Y. Guo, J. Gu, Interfacial thermal resistance in thermally conductive polymer composites: a review, Compos. Commun. 22 (2020), https://doi.org/10.1016/j.coco.2020.100518.

[44] Y. Guo, K. Ruan, X. Shi, X. Yang, J. Gu, Factors affecting thermal conductivities of the polymers and polymer composites: a review, Compos. Sci. Technol. 193 (2020), https://doi.org/10.1016/j.compscitech.2020.108134.
[45] M. Kim, D. Park, J. Kim, A comprehensive exploration of PPS/MgO@MoS2 core–shell composites for enhanced thermal and mechanical performance, J. Mater. Res. Technol. 30 (2024) 9337–9342, https://doi.org/10.1016/j.jmrt.2024.06.021.
[46] Y. Seki, E. Kizilkan, B.M. Leşkeri, M. Sarikanat, L. Altay, A. Isbilir, Comparison of the thermal and mechanical properties of poly(phenylene sulfide) and poly (phenylene sulfide)-syndiotactic polystyrene-based thermal conductive composites, ACS Omega 7 (2022) 45518–45526, https://doi.org/10.1021/acsomega.2c06152.
[47] A. Zhou, Z. Yu, H. Wei, L.H. Tam, T. Liu, D. Zou, Understanding the toughening mechanism of silane coupling agents in the interfacial bonding in steel fiber-reinforced cementitious composites, ACS Appl. Mater. Interfaces 12 (2020) 44163–44171, https://doi.org/10.1021/acsami.0c12477.
[48] A.B. Azizah, H.D. Rozman, A.A. Azniwati, G.S. Tay, The effect of filler loading and silane treatment on kenaf core reinforced polyurethane composites: mechanical and thermal properties, J. Polym. Environ. 28 (2020) 517–531, https://doi.org/10.1007/s10924-019-01623-8.
[49] P. Jantachum, B. Khumpaitool, S. Utara, Effect of silane coupling agent and cellulose nanocrystals loading on the properties of acrylonitrile butadiene rubber/natural rubber nanocomposites, Ind. Crops Prod. 195 (2023), https://doi.org/10.1016/j.indcrop.2023.116407.
[50] P. Nuinu, C. Sirisinha, K. Suchiva, P. Daniel, P. Phinyocheep, Improvement of mechanical and dynamic properties of high silica filled epoxide functionalized natural rubber, J. Mater. Res. Technol. 24 (2023) 2155–2168, https://doi.org/10.1016/j.jmrt.2023.03.101.
[51] Y. Ma, H. Huang, H. Zhou, M. Graham, J. Smith, X. Sheng, et al., Superior anti-corrosion and self-healing bi-functional polymer composite coatings with polydopamine modified mesoporous silica/graphene oxide, J. Mater. Sci. Technol. 95 (2021) 95–104, https://doi.org/10.1016/j.jmst.2021.04.019.
[52] D. Yang, L. Yu, J. Ai, Q. Wei, Y. Ni, L. Zhang, Enhanced thermal conductivity of carboxyl nitrile butadiene rubber composites with low-cost poly(catechol/polyamine) modified Al2O3 via biomimetic method, Compos. Commun. 23 (2021), https://doi.org/10.1016/j.coco.2020.100565.
[53] X. Wang, Z. Luo, Y. Xu, J. Zhong, H. Zhang, J. Liang, Preparation and performance of natural rubber latex treatment for silica filled natural rubber composites, J. Appl. Polym. Sci. 140 (2023), https://doi.org/10.1002/app.53966.
[54] D. Yang, Q. Wei, L. Yu, Y. Ni, L. Zhang, Natural rubber composites with enhanced thermal conductivity fabricated via modification of boron nitride by covalent and non-covalent interactions, Compos. Sci. Technol. 202 (2021), https://doi.org/10.1016/j.compscitech.2020.108590.
[55] X. Xie, D. Yang, Multi-functionalization of Al2O3 nanoparticles for enhancing thermal conductivity of epoxy natural rubber composites, Appl. Surf. Sci. 602 (2022), https://doi.org/10.1016/j.apsusc.2022.154335.
[56] D. Yang, Q. Wei, L. Yu, Y. Ni, L. Zhang, Natural rubber composites with enhanced thermal conductivity fabricated via modification of boron nitride by covalent and non-covalent interactions, Compos. Sci. Technol. 202 (2021), https://doi.org/10.1016/j.compscitech.2020.108590.
[57] J. Zeng, Y.J. Li, Y.C. Lu, Y.P. Li, H.P. Liu, C.X. Wu, et al., Preparation of Bi2O3@PCPA-KH590/chloroprene composites with good mechanical properties under high-filling, J. Appl. Polym. Sci. 141 (2024), https://doi.org/10.1002/app.54782.
[58] W. Ye, Z. Ye, T. Liang, X. Zeng, Z. Wen, L. Ren, et al., Stretchable thermal interface materials by tailoring the chain relaxation at the filler/polymer interface, ACS Appl. Polym. Mater. 4 (2022) 4653–4663, https://doi.org/10.1021/acsapm.1c01871.
[59] Z. Cheng, W. Xu, D. Ding, C. Xu, Y. Xie, M. Qiao, Preparation of boron nitride hybrid containing phosphorus and silicon and its effect on flame retardant, smoke suppression, and thermal conductivity properties of styrene-butadiene rubber, J. Appl. Polym. Sci. 139 (2022), https://doi.org/10.1002/app.53071.
[60] W. Ye, Z. Ye, T. Liang, X. Zeng, Z. Wen, L. Ren, et al., Stretchable thermal interface materials by tailoring the chain relaxation at the filler/polymer interface, ACS Appl. Polym. Mater. 4 (2022) 4653–4663, https://doi.org/10.1021/acsapm.1c01871.
[61] N. Ab Rasid, R. Alawi, Y. Johari, N.A.A. Muttlib, M.H. Hussin, D. Mohamad, et al., Effect of surface treatment hybridization of kenaf nanocellulose on the thermal stability and mechanical properties of rice husk nanohybrid dental composite, Cellulose 31 (2024) 7437–7448, https://doi.org/10.1007/s10570-024-06051-z.
[62] B. Yu, Y. Zhou, Z. Luo, J. Fan, J. He, Y. Liu, et al., Highly thermally conductive flexible insulated PI/BNNS@rGO nanocomposite paper with a three-dimensional network bridge structure, Appl. Surf. Sci. 630 (2023), https://doi.org/10.1016/j.apsusc.2023.157457.
[63] H. Ribeiro, J.P.C. Trigueiro, M.C. Lopes, J.J. Pedrotti, C.F. Woellner, W.M. Silva, et al., Enhanced thermal conductivity and mechanical properties of hybrid MoS2/h-BN polyurethane nanocomposites, J. Appl. Polym. Sci. 135 (2018), https://doi.org/10.1002/app.46560.
[64] C. Yue, L. Guan, X. Zhang, Y. Wang, L. Weng, Thermally conductive epoxy/boron nitride composites with high glass transition temperatures for thermal interface materials, Mater. Des. 212 (2021), https://doi.org/10.1016/j.matdes.2021.110190.
[65] P. Wang, L. Yang, S. Gao, X. Chen, T. Cao, C. Wang, et al., Enhanced dielectric properties of high glass transition temperature PDCPD/CNT composites by frontal ring-opening metathesis polymerization, Adv. Compos. Hybrid Mater. 4 (2021) 639–646, https://doi.org/10.1007/s42114-021-00287-0.
[66] Z.B. Zhao, J.D. Liu, X.Y. Du, Z.Y. Wang, C. Zhang, S.F. Ming, Fabrication of silver nanoparticles/copper nanoparticles jointly decorated nitride flakes to improve the thermal conductivity of polymer composites, Colloids Surf. A Physicochem. Eng. Asp. 635 (2022), https://doi.org/10.1016/j.colsurfa.2021.128104.
[67] Q. Wei, Y. Ni, D. Yang, L. Yu, L. Zhang, Enhanced thermal conductivity of silicone rubber via synergistic effects of polydopamine modification and silver deposition on boron nitride, Compos. Commun. 30 (2022), https://doi.org/10.1016/j.coco.2022.101082.
[68] X. Xie, D. Yang, Multi-functionalization of Al2O3 nanoparticles for enhancing thermal conductivity of epoxy natural rubber composites, Appl. Surf. Sci. 602 (2022), https://doi.org/10.1016/j.apsusc.2022.154335.
[69] C. Yue, L. Zhao, L. Guan, X. Zhang, C. Qu, D. Wang, et al., Vitrimeric silicone composite with high thermal conductivity and high repairing efficiency as thermal interface materials, J. Colloid Interface Sci. 620 (2022) 273–283, https://doi.org/10.1016/j.jcis.2022.04.017.
[70] Y. Zhang, Y. Fan, U. Kamran, S.J. Park, Improved thermal conductivity and mechanical property of mercapto group-activated boron nitride/elastomer composites for thermal management, Compos Part A Appl Sci Manuf 156 (2022), https://doi.org/10.1016/j.compositesa.2022.106869.
[71] L.H. Zhao, L. Wang, Y.F. Jin, J.W. Ren, Z. Wang, L.C. Jia, Simultaneously improved thermal conductivity and mechanical properties of boron nitride nanosheets/aramid nanofiber films by constructing multilayer gradient structure, Compos. B Eng. 229 (2022), https://doi.org/10.1016/j.compositesb.2021.109454.
[72] L.P. Lim, J.C. Juan, N.M. Huang, L.K. Goh, F.P. Leng, Y.Y. Loh, Enhanced tensile strength and thermal conductivity of natural rubber graphene composite properties via rubber-graphene interaction, Mater. Sci. Eng., B 246 (2019) 112–119, https://doi.org/10.1016/j.mseb.2019.06.004.
[73] C. Chen, Y. Xue, Z. Li, Y. Wen, X. Li, F. Wu, et al., Construction of 3D boron nitride nanosheets/silver networks in epoxy-based composites with high thermal conductivity via in-situ sintering of silver nanoparticles, Chem. Eng. J. 369 (2019) 1150–1160, https://doi.org/10.1016/j.cej.2019.03.150.
[74] X. Yang, Y. Guo, Y. Han, Y. Li, T. Ma, M. Chen, et al., Significant improvement of thermal conductivities for BNNS/PVA composite films via electrospinning followed by hot-pressing technology, Compos. B Eng. 175 (2019), https://doi.org/10.1016/j.compositesb.2019.107070.